Properties of the Speckle of Focused, Phase-Converted Laser Beams and the Reduction of Time-Averaged Irradiation Nonuniformity in Laser-Driven Plasmas due to Target Ablation

Highly uniform irradiation and energy absorption at the surface of fuel-filled capsules are among the most important requirements for successful inertial confinement fusion (ICF) implosions.[1,2] In most laser-plasma experiments of interest to ICF, laser beams are phase converted by being passed through distributed phase plates (DPP's).[3] DPP's greatly improve the uniformity of focused beams by reducing large-scale beam structure, leaving intensity profiles with well-controlled, reproducible envelopes modulated by fine speckle.[3,4] However, the nonuniformity remaining in the speckle is still more than the maximum allowable nonuniformity for ICF. This article presents an analytical model of this speckle and uses this model to show how a uniformly ablating plasma atmosphere acts to reduce the contribution of the speckle to the effective, time-averaged irradiation nonuniformity.

DPP's are transparent plates divided into a large number of flat area elements that are all identical, except that each of them adds a random phase delay to the transmitted light. This random distribution of phase delays effectively divides the beam into mutually spatially incoherent beamlets. When the beam is focused onto a surface, the irradiation pattern is a superposition of all the beamlets, where the envelope of the total intensity distribution is the same as the envelope of each individual beamlet. The shape and size of this envelope are determined by the shape and size of the individual phase-plate area element. The speckle in the intensity profile is the result of the mutual interference of the beamlets. The random spatial correlation among all beamlet phases results in a speckle modulation spectrum that is much flatter than would be obtained from a beam without DPP's, where the strong short-range spatial correlations in the beam phase profile result in correspondingly strong long-scale structure in the focused intensity pattern. DPP's with continuous phase distributions have been developed recently. They function with the same effect as discrete DPP's, except that their focused intensity profiles do not have the side lobes characteristic of the discrete area elements of discrete DPP's, and appreciably more of the laser energy can be focused onto a spherical target.[5]

This article shows that the effects of the speckle in the intensity distribution within a plasma average out in time due to a number of optical and hydrodynamic effects of uniform ablation that cause the irradiation-intensity distribution to move relative to the plasma. Any local effect of the irradiation speckle on the plasma that is cumulative, such as the conversion of laser intensity peaks into thermal energy peaks by absorption, will be reduced in proportion to this time averaging. The most direct measure of irradiation uniformity is that of the intensity distribution at a given surface, such as a surface fixed in space or a surface of constant electron density near where laser energy is absorbed. All effects that cause the irradiation-intensity distribution to move relative to this surface will contribute to a reduction in the effective irradiation nonuniformity by time averaging.

A number of laser-system modifications have been developed that cause the speckle to change rapidly in time so that their effects on the plasma will average out in time. These include induced spatial incoherence (ISI),[6] where the temporal coherence of the laser beam is disrupted, and smoothing by spectral dispersion (SSD),[7] where the laser is modulated electro-optically to expand the bandwidth of the laser. With both ISI[6,8] and SSD,[9,10] significant reduction in the effects of irradiation nonuniformity has been obtained, certainly more than the reduction that can be attributed to ablation-induced effects alone. Progress in developing these techniques has been driven in large part by the need to shorten their averaging times so that the cumulative effects of the irradiation nonuniformity can be averaged away very early in the pulse, before they can be imprinted irreversibly on the target.[10,11] Consequently, the possibility of additional speckle averaging at early times by all possible means remains an important question.

One source of averaging due to ablation is the continuous accumulation of ablated plasma in the beam path between the laser and the surface where the uniformity is measured. The dispersive effect of the ablated plasma reduces the total phase of light propagating through it between any two fixed points,

and the resulting refraction foreshortens the speckled interference pattern along the axial direction so that it appears to have receded from the target, back toward the laser. The continuous feeding of the atmosphere by ablation from the target results in a continuously increasing phase reduction and refraction, resulting in a steady recession of the intensity distribution past any surface fixed in the plasma at a point of constant electron density. The hydrodynamic motion of the plasma makes a comparably important contribution to the total motion of the intensity distribution relative to this surface. Both effects have been identified by Dewandre *et al.*[12] as sources of the frequency shift of light reflected from the atmosphere of an ablating target. These ablation-induced time-averaging effects are interesting not only because they are potentially beneficial, but also because they are unavoidable consequences of ablation that must be considered in interpreting any ICF experiment, past and future, where the quantitative effects of irradiation nonuniformity are a matter of concern.

For the purposes of this article, irradiation uniformity will be considered to be the uniformity of the intensity distribution at the absorption surface, which is defined simply as a surface of constant electron density, n_{abs}, where the absorption occurs. Absorption does occur over a finite distance, however, and some degree of additional smoothing of the effects of the irradiation nonuniformity can be expected since an appropriately weighted, instantaneous spatial average of the absorbed intensity distribution over this distance is a better measure of the true effective nonuniformity. Identifying this weighting would take this article beyond its intended subject of irradiation uniformity to the problem of relating the uniformity of ablative drive to the irradiation uniformity.

Thermal conduction and radiative transport in the atmosphere of an ablating target are other processes that smooth the nonuniformities in the thermal-energy distribution that are driven by nonuniform energy deposition.[1,13,14] These smoothing mechanisms can be effective only in the presence of a plasma atmosphere where there is a separation between the absorption region and the ablation region, where the pressure gradient driving the ablation is concentrated. Consequently, neither of these effects can smooth nonuniformities at the beginning of the laser pulse before an atmosphere has developed. It has been suggested that a suitable atmosphere could be formed by a flash of x rays applied before the laser pulse[15] or by coating the outside of the target with a thick outer layer of very light polymer foam.[16] A crucial advantage of ablation-induced time averaging of speckle over thermal smoothing and instantaneous axial averaging over an absorption interval is that it does not require that an atmosphere be present initially, only that one has begun to form.

This article first develops an analytical model for the intensity distribution and the spatial spectrum of the speckle pattern in the focal region for the case of random DPP's with discrete phase elements. The paraxial approximation is applied to the beam propagation in a uniform plane-parallel atmosphere. In this model, the reduction in the speckle spectrum due to averaging over an interval of time at a given absorption surface is equivalent to a spatial average over the corresponding interval of the propagation axis that represents the thickness of the portion of the intensity profile that would have passed through the absorption surface during the given time interval.

A simple idealized atmosphere model is used to obtain estimates of various contributions to this averaging interval. The plasma contribution is considered separately, and it is seen that the accumulation of typical ablation plasmas over typical hydrodynamic scale times can displace the speckle distribution over distances that are significant on the scale of the speckle structure. The total of the hydrodynamic and plasma effects is calculated in terms of a planar target accelerated by the expansion of an isothermal atmosphere. From this, it is seen that the plasma and hydrodynamic effects tend to cancel each other in a solid target during the beginning of the ablation, which is the crucial period when the atmosphere is most susceptible to a permanent imprint of the irradiation nonuniformity. The rates at which these averaging effects occur are calculated using 1-D hydrocode simulations of the ablation of a planar target for a range of irradiation intensities. These numerical results are well fit by the analytical approximations, which verifies that the analytical results are applicable. The averaging rates are the crucial final result because useful speckle averaging requires that the intensity nonuniformities must move through the plasma quickly enough to limit their cumulative, irreversible effects.

It is found that the averaging times in a solid CH target due to the plasma and hydrodynamic effects vary with the irradiation intensity and can be as little as a few hundred picoseconds for a beam of $f/7$ focal ratio, 0.351-μm wavelength, and 10^{15} W/cm^2 intensity. This smoothing time is short, compared with the hydrodynamic time scales of ICF implosions, but not short enough to avoid a permanent imprint of the irradiation nonuniformity on the plasma. While the plasma and hydrodynamic effects counteract each other early in the pulse, the hydrodynamic effect reverses at later times, as the target

accelerates, and the two effects add constructively, giving a much larger effect. Even then, the total averaging effect remains much slower than SSD and ISI smoothing times.

Many ICF experiments have already shown that ISI[6,8] and SSD[9,10] significantly reduce the effects of irradiation nonuniformity. The results of these experiments imply that any ablative smoothing effects that might have occurred in these experiments were dominated by SSD or ISI, but they do not rule out that ablative effects were important enough to have affected the quantitative comparisons between the results of measurements made with and without ISI or SSD. In the absence of SSD and ISI, it is likely that the ablative effects are an important smoothing mechanism, and they should be considered in interpreting experiments intended to determine the beneficial effects of these laser-system smoothing techniques. The main conclusion to be drawn from this work is that the formation of an ablated plasma atmosphere does act to reduce the effects of radiation nonuniformity and that understanding these effects is essential to a complete quantitative understanding of the effects of irradiation nonuniformity on these plasmas.

Beam Speckle Modulation Spectrum in the Focal Region

1. Derivation of the Beam Speckle Modulation Spectrum

The first task is to solve the electromagnetic wave equation

$$\left[\frac{\partial^2}{\partial t^2} - c^2\nabla^2 + \omega_p^2(z)\right]\mathbf{E}(\mathbf{x},t) = 0 \tag{1}$$

for a monochromatic beam of frequency ω focused onto a plane-parallel plasma target whose electron density $n_e(\mathbf{x}) = n_e(z)$ varies in the axial direction, the z direction, normal to the target surface. In what follows, the electron plasma frequency $\omega_p(z)$ will be expressed as

$$\omega_p^2(z) = \omega^2\,\frac{n_e(z)}{n_c(\omega)}, \tag{2}$$

in terms of the critical electron density $n_c(\omega)$. Using the paraxial approximation, a solution to Eq. (1) can be obtained in terms of the reduced field quantity $\mathbf{U}(\mathbf{x})$, which represents the electrical field $\mathbf{E}(\mathbf{x})$ with the axial-wave phase removed,

$$\mathbf{E}(\mathbf{x},t) = \mathbf{U}(\mathbf{x})\exp\left[i\int_0^z k(z')\,dz' - i\omega t\right]. \tag{3}$$

The reduced field can be used to calculate the intensity of the irradiation,

$$I(\mathbf{x}) = |\mathbf{U}(\mathbf{x})|^2. \tag{4}$$

The wave vector of the axial wave $k(z)$ obeys the dispersion relation

$$c^2\,k^2(z) = \omega^2 - \omega_p^2(z) \tag{5}$$

for a plane wave in an unmagnetized plasma. Note that the ω dependence of n_c and the z dependence of n_e and k will not always be written, but they are always understood to apply.

For the present purpose, the paraxial approximation is the assumption that nearly all the z dependence of $\mathbf{E}(\mathbf{x})$ is contained in the axial phase factor of Eq. (3), rather than in $\mathbf{U}(\mathbf{x})$, so that

$$\left|\frac{\partial^2\mathbf{U}}{\partial z^2}\right| << k\left|\frac{\partial\mathbf{U}}{\partial z}\right|. \tag{6}$$

Using Eqs. (3), (5), and (6), the paraxial-wave equation,

$$\nabla_\perp^2\mathbf{U} + 2\,i\,k\,\frac{\partial\mathbf{U}}{\partial z} + i\,\frac{\partial k}{\partial z}\mathbf{U} = 0, \tag{7a}$$

where

$$\nabla_\perp^2 = \frac{\partial^2}{\partial x^2} + \frac{\partial^2}{\partial y^2}, \tag{7b}$$

is obtained from the full-wave equation, Eq. (1).

The desired solution to Eqs. (7) is that of a beam of total power P, emerging through a planar aperture of area A oriented normal to the z axis. The beam is focused at the aperture with a device of focal length z_0 so that it converges all the way from the aperture plane, which intersects the z axis at the point $\mathbf{x} = (0,0,-z_0)$, to the focal point at the origin of the coordinates, $\mathbf{x} = 0$. This solution can be written in the form of an integral sum of converging waves,

$$U(\mathbf{x}) = \frac{k_v}{2\pi z_0}\sqrt{\frac{k_v}{k}\frac{P}{A}}\iint_A W(\mathbf{q}) \times\exp\left\{-i\left[\frac{k_v}{z_0}\mathbf{q}\cdot\mathbf{x} + \frac{k_v\,q^2\,\zeta(z)}{2\,z_0^2} + \phi(\mathbf{q})\right]\right\}d^2q. \tag{8}$$

It is assumed that the field at the aperture is uniformly polarized. As a result, the field at the point $\mathbf{x}$ is identically polarized

everywhere, and polarization can be removed from the expression for the focused field, leaving Eq. (8) as a scalar expression. The vector variable $\mathbf{q}$ represents a point on the aperture. The vacuum wave number of a plane wave of frequency ω is $k_v = \omega/c$. The function $\zeta(z)$ is given by

$$\zeta(z) = \int_0^z \frac{k_v}{k(z')}\, dz' \tag{9}$$

and is the only z-dependent quantity in the phase of the solution. It is a measure of distance along the beam axis from the focal point that reduces to $\zeta(z) = z$ in a vacuum. In all expressions below, where the distance measure $\zeta(z)$ is written as ζ, its z dependence is understood. The boundary conditions of this solution are the function $W(\mathbf{q})$, the amplitude distribution in the aperture plane, which is real, positive, and normalized so that

$$\iint_A W^2(\mathbf{q})\, d^2q = A, \tag{10}$$

and $\phi(\mathbf{q})$, which contains all the phase information in the beam at the aperture, including the intrinsic phase distribution of the beam plus the segmented phase profile added by the DPP.

The integral in Eq. (8) can be written as a sum of integrals over the N individual, identical, and identically oriented area elements that completely fill the aperture. Mathematically, this is a useful simplification because the phase $\phi(\mathbf{q})$ varies randomly and abruptly from element to element. Physically, this represents the beam as an array of beamlets of mutually spatially incoherent phase. The solution, written in this way, is

$$\begin{aligned} U(\mathbf{x}) \;=\; & \frac{k_v}{2\pi z_0}\sqrt{\frac{k_v}{k}\frac{P}{A}}\sum_{j=1}^{N} W\left(\mathbf{q}_j - \mathbf{q}_0\right) \\ & \times \exp\left\{-i\left[\frac{k_v}{z_0}\mathbf{q}_j \cdot \mathbf{x} + \frac{k_v\, q_j^2\, \zeta}{2 z_0^2} + \phi\left(\mathbf{q}_j\right)\right]\right\} \\ & \times \iint_{a_j} \exp\left\{-i\left[\frac{k_v}{z_0}\boldsymbol{\xi}\cdot\mathbf{x} \right.\right. \\ & \left.\left. + \frac{k_v\,\zeta}{z_0^2}\mathbf{q}_j\cdot\boldsymbol{\xi} + \frac{k_v\,\xi^2\,\zeta}{2 z_0^2}\right]\right\} d^2\xi\,, \end{aligned} \tag{11}$$

where each element is of area $a_j = a = A/N$. The substitution $\mathbf{q} = \mathbf{q}_j + \xi$ has been made, where the constant $\mathbf{q}_j$ denotes the center point of the jth DPP element. It is assumed that both $W(\mathbf{q})$ and $\phi(\mathbf{q})$ vary slowly enough within each DPP element to be approximated as the constants W_j and ϕ_j, respectively. Thus far no restriction has been placed on the distribution $W(\mathbf{q})$, other than that it must vanish for $\mathbf{q}_j$ large enough to cause Eq. (11) to violate the paraxial condition stated by Eq. (6). It is now assumed that $W(\mathbf{q}')$ describes a distribution centered at $\mathbf{q}' = 0$ so that Eq. (11), written as shown in terms of $W\left(\mathbf{q} - \mathbf{q}_0\right)$, represents a beam that originates from an illumination distribution on the aperture plane, centered off-axis at a point $\mathbf{q}_0$, and converges to a focal point on the z axis. This displacement $\mathbf{q}_0$ corresponds to an angle of incidence $\psi = \tan^{-1}\left(q_0/z_0\right)$, where $q_0 = |\mathbf{q}_0|$, or $\psi \cong q_0/z_0$ for small angles within the paraxial approximation, $q_0 << z_0$.

Equation (11) can be simplified by discarding negligible terms. What remains is

$$\begin{aligned} U(\mathbf{x}) \;=\; & \frac{k_v}{2\pi z_0}\sqrt{\frac{k_v}{k}\frac{P}{A}}\iint_a \exp\left\{-i\left[\frac{k_v}{z_0}\boldsymbol{\xi}\cdot\mathbf{x}\right]\right\} d^2\xi \\ & \times \sum_{j=1}^{N} W_j \exp\left\{-i\left[\frac{k_v}{z_0}\left(\mathbf{q}_j + \mathbf{q}_0\right)\cdot\mathbf{x} \right.\right. \\ & \left.\left. + \frac{k_v\left(q_j^2 + 2\,\mathbf{q}_j\cdot\mathbf{q}_0 + q_0^2\right)\zeta}{2 z_0^2} + \phi_j\right]\right\}. \end{aligned} \tag{12}$$

The transform $\mathbf{q} \rightarrow \mathbf{q} + \mathbf{q}_0$ has been made from coordinates centered at the z axis to coordinates centered at the center of the beam on the aperture plane, so that the set of all $\mathbf{q}_j$ is centered about the origin $\mathbf{q} = 0$ and so that $\mathbf{q}_0$ represents the displacement of the entire beam from normal incidence.

The restriction of the paraxial approximation on Eqs. (8), (11), and (12), as stated by Eq. (6), requires that the focal convergence of the beam be slow and that the angle of incidence be small. This implies that the beam must not be followed into the plasma too close to what would be the turning point of any ray in a geometrical-optics ray-tracing treatment of the same problem. A clearer statement of a condition that is sufficient to satisfy Eq. (6) can be obtained using Eqs. (9) and (12). This is

$$\frac{k_v\left(q_j^2 + 2\,\mathbf{q}_j\cdot\mathbf{q}_0 + q_0^2\right)}{2 z_0^2}\frac{k_v}{k} << k \tag{13}$$

for all j. The meaning of this condition is made adequately clear by considering the case of a circular aperture of radius R, which gives

$$\frac{(R+q_0)^2}{2z_0^2} << \left(1-\frac{n_e}{n_c}\right), \tag{14a}$$

or, writing this in terms of the angle of incidence $\psi \cong q_0/z_0$ and the focal ratio or f-number of the beam $f = z_0/2R$,

$$\left(\frac{1}{2f}+\psi\right)^2 << 2\left(1-\frac{n_e}{n_c}\right). \tag{14b}$$

Equations (14) are essentially the same as the condition that no ray in the laser beam should approach its turning point. This turning point can be identified for each component of the plane-wave decomposition expressed in Eq. (12) as the point where the wave vector has become purely transverse. The transverse component $\mathbf{k}_\perp$ of the wave vector $\mathbf{k}$ of each component of the plane-wave decomposition of the reduced field can be identified in Eq. (12) as

$$\mathbf{k}_\perp = \frac{k_\nu}{z_0}(\mathbf{q}+\mathbf{q}_0). \tag{15}$$

As the beam propagates deeper into the plasma, $n_e(z)$ increases and k^2 decreases to the point where $\mathbf{k} = \mathbf{k}_\perp$, which defines the turning-point electron density n_{turn}. Combining Eqs. (2), (5), and (15), the turning-point density for the most obliquely incident ray is

$$\frac{n_{\text{turn}}}{n_c} = 1-\left(\frac{1}{2f}+\psi\right)^2 \tag{16}$$

for the case of a circular aperture. Even though the more normally incident rays penetrate further than this, it is clear that the paraxial approximation for the treatment of the whole beam has become invalid at $n_e = n_{\text{turn}}$. For the present purposes, either the condition $n_e < n_{\text{turn}}$ or Eqs. (14) can be taken as a validity condition. A more thorough validity study will not be undertaken here.

Equation (12) can be used in Eq. (4) to obtain the intensity, which can be written as the product

$$I(\mathbf{x}) = N\, I_0(\mathbf{x})\, G(\mathbf{x}), \tag{17}$$

where $I_0(\mathbf{x})$ is the intensity profile of a single beamlet,

$$I_0(\mathbf{x}) = \frac{(P/A)}{4\pi^2}\left(\frac{k_\nu}{k}\right)\left(\frac{k_\nu a}{z_0}\right)^2 \left|\frac{1}{a}\iint_a \exp\left\{-i\frac{k_\nu}{z_0}\boldsymbol{\xi}\cdot\mathbf{x}\right\} d^2\xi\right|^2, \tag{18}$$

and where $G(\mathbf{x})$ is the speckle modulation factor

$$G(\mathbf{x}) = \frac{1}{N}\sum_{j=1}^{N} W_j^2 + \frac{1}{N}\sum_{j=1}^{N}\sum_{k\neq j}^{N} W_j W_k \exp\left\{-i\left[\Delta\phi_{jk} + \frac{k_\nu}{z_0}\Delta\mathbf{q}_{jk}\cdot\mathbf{x} + \frac{k_\nu \zeta}{z_0^2}\left(\bar{\mathbf{q}}_{jk}+\mathbf{q}_0\right)\cdot\Delta\mathbf{q}_{jk}\right]\right\}. \tag{19}$$

The factors in Eq. (18), the beam envelope expression, have been grouped so that they are all dimensionless, except for the intensity P/A.

The first term of the modulation factor given by Eq. (19) represents all the identical noninterfering pairs and is simplified by using the discrete-sum equivalent of Eq. (10),

$$\frac{1}{N}\sum_{j=1}^{N} W_j^2 = 1. \tag{20}$$

The second term in Eq. (19) is the sum of interference terms that represent the speckle modulation. For each element pair (j,k), there is a phase difference $\Delta\phi_{jk} = \phi_j - \phi_k$, a mean position $2\bar{\mathbf{q}}_{jk} = \mathbf{q}_j + \mathbf{q}_k$, and a separation $\Delta\mathbf{q}_{jk} = \mathbf{q}_j - \mathbf{q}_j$. Since the set of the positions of the DPP element centers $\{\mathbf{q}_j\}$ forms a regular lattice, a particular separation vector $\Delta\mathbf{q}_{jk}$ occurs repeatedly. Let N_p, then, be the number of distinct separation vectors, let $\Delta\mathbf{q}_m$ be a particular one among them, and let $N(\Delta\mathbf{q}_m)$, abbreviated by N_m when convenient, be the number of element pairs that have the separation $\Delta\mathbf{q}_m$. Any one of the N_m different pairs of points that share a particular $\Delta\mathbf{q}_m$ can be distinguished because they all have distinct $\bar{\mathbf{q}}_{jk}$, each of which can be denoted as $\bar{\mathbf{q}}_n$. The element pairs can now be identified by the indices (m,n), as well as (j,k), so each $\Delta\phi_{jk}$ can also be denoted as $\Delta\phi_{mn}$, and similarly, W_jW_k is a particular element (m,n) of the matrix formed by the outer product $\mathbf{W}\otimes\mathbf{W}$. From this point on, the analysis will assume uniform illumination of the beam aperture so that $W_j = 1$. The modulation function can

now be written as

$$G(\mathbf{x}) = 1 + \sum_{m=2}^{N_p} C(\Delta\mathbf{q}_m, \zeta) \exp\left[-i \frac{k_\nu}{z_0} \Delta\mathbf{q}_m \cdot \mathbf{x}\right], \quad (21a)$$

where

$$C(\Delta\mathbf{q}_m, \zeta) = \frac{1}{N} \sum_{n=1}^{N_m} \exp\left\{-i\left[\Delta\phi_{mn} + \frac{k_\nu \zeta}{z_0^2}(\bar{\mathbf{q}}_n + \mathbf{q}_0) \cdot \Delta\mathbf{q}_m\right]\right\}. \quad (21b)$$

From the set of all possible $\Delta\mathbf{q}_m$, $m = 1$ is chosen for $\Delta\mathbf{q} = 0$, which is excluded from the sum in Eq. (21a), since all $\Delta\mathbf{q} = 0$ pairs have already been summed to obtain the first term.

2. Evaluation of the Speckle Modulation Spectrum

Equation (21a) expresses the speckle modulation as a Fourier series whose coefficients, given by Eq. (21b), can also be expressed as a correlation sum

$$C(\Delta\mathbf{q}_m, \zeta) = \frac{1}{N} \sum_{n=1}^{N_m} f\left(\bar{\mathbf{q}}_n + \frac{1}{2}\Delta\mathbf{q}_m, \zeta\right) f^*\left(\bar{\mathbf{q}}_n - \frac{1}{2}\Delta\mathbf{q}_m, \zeta\right) \quad (22a)$$

of the function

$$f(\mathbf{q}, \zeta) = \exp\left\{-i\left[\frac{k_\nu |\mathbf{q} + \mathbf{q}_0|^2 \zeta}{2 z_0^2} + \phi(\mathbf{q})\right]\right\}. \quad (22b)$$

As was stated earlier, $\phi(\mathbf{q})$ is uniformly random over the interval $[0, 2\pi]$, from element to element on the DPP, or from term to term in the sum in Eq. (22a). In this section, the speckle modulation is being calculated at a single instant or at a fixed value of ζ, so the entire exponent in Eq. (22b) has the statistical properties of a uniformly random phase. Therefore, at any one target plane and at one particular spatial frequency $\mathbf{K}_m$, where

$$\mathbf{K}_m = \frac{k_\nu}{z_0} \Delta\mathbf{q}_m, \quad (23)$$

the contribution to the speckle modulation is given by a correlation sum of random phases, which gives

$$N^2 \left\langle \left| C(\Delta\mathbf{q}_m) \right|^2 \right\rangle = N_m. \quad (24)$$

This is obtained from Eqs. (22) by recognizing that the amplitude of a sum of terms of random phase accumulates as the quadrature sum of the amplitudes of the terms, just as the total distance in a random walk accumulates as the square root of the number of steps.[17] It should not be forgotten that Eq. (24) pertains to random-phase DPP's. The speckle modulation can be appreciably less than that suggested by Eq. (24) if the DPP is constructed with a nonrandom pattern whose spatial correlation function is less than random. If the phase imperfections of the laser beam are small enough, then irradiation uniformity can be improved simply by choosing the DPP pattern appropriately.[18]

According to the estimate stated in Eq. (24), the spectral density of the modulation pattern at a spatial frequency $\mathbf{K}_m$ is determined by N_m, the number of DPP element pairs within the aperture A that are separated by the vector $\Delta\mathbf{q}_m$. One method of counting all such pairs is illustrated by Fig. 68.18. Figure 68.18(a) shows an aperture A with center point O where one pair of area elements is represented by points J and K. Figure 68.18(b) shows this same aperture along with an exact duplicate A', which is obtained by moving every point in A by the displacement $\Delta\mathbf{q}_m$. For every point P in A, there is a point P' in A'. Note in particular that this displacement brings point K to K', which is congruent to J, and that this point is within $A \cap A'$, the intersection of A and A'. Similarly, any other pair of points within A with the same separation $\Delta\mathbf{q}_m$ corresponds, one-to-one, with a single point in $A \cap A'$. Therefore, the number of element pairs in A separated by the displacement $\Delta\mathbf{q}_m$ is the area of $A \cap A'$ divided by $a = A/N$, the area of a single element, or

$$N(\Delta\mathbf{q}_m) = \iint_{A \cap A'} \frac{d^2\bar{q}}{a}. \quad (25)$$

Equation (25) is an exact result. Writing the quantity $N(\Delta\mathbf{q}_m)$ as a function of $\Delta\mathbf{q}_m$ facilitates the transition from a function whose domain consists of a discrete set of vectors $\{\Delta\mathbf{q}_m\}$ to $N(\Delta\mathbf{q})$, a function of a continuous vector variable $\Delta\mathbf{q}$.

The result obtained from Eqs. (24) and (25) for a circular aperture of radius R is

$$\left\langle \left| C(\Delta q) \right|^2 \right\rangle = \frac{2}{\pi N}\left[\cos^{-1}\left(\frac{\Delta q}{2R}\right) - \left(\frac{\Delta q}{2R}\right)\sqrt{1 - \left(\frac{\Delta q}{2R}\right)^2}\right], \quad (26a)$$

where $\Delta q = |\Delta\mathbf{q}|$ and

$$\Delta q \le 2R. \quad (26b)$$

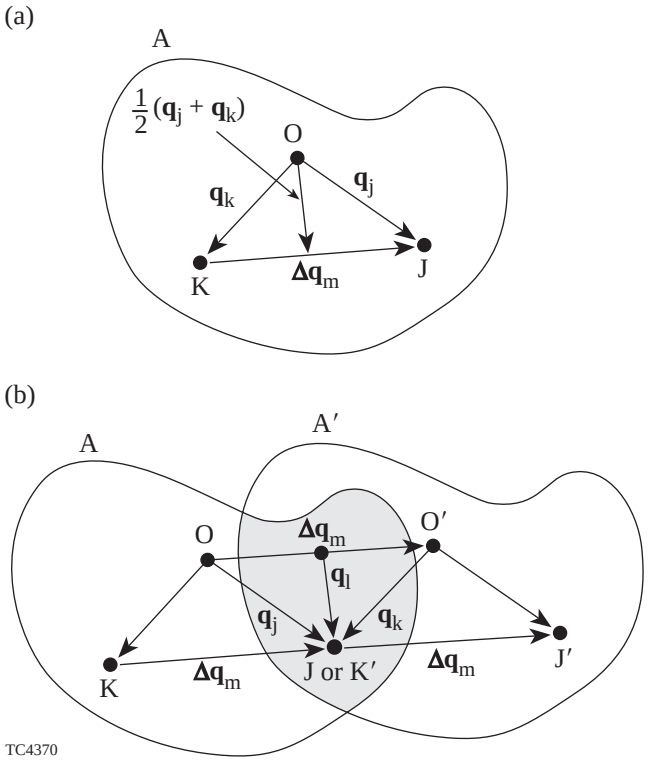

Figure 68.18
The spectral intensity of the speckle pattern at a spatial frequency $\mathbf{K}_m$ is determined by the number of DPP element pairs within an aperture A in the DPP plane that are separated by the vector $\Delta\mathbf{q}_m$. Counting these pairs is simplified by noting that each pair within an aperture A, points J and K as shown here, for example, corresponds, one-to-one, with a point L within the intersection of A and an identical aperture A' obtained from A by a displacement $\Delta\mathbf{q}_m$. This displacement brings any point P to P'. In particular, point J is congruent to point K', both of which are equivalent to the point L. The measure of the spectral intensity of the speckle at spatial frequency $\mathbf{K}_m$ is the area of the intersection of A and A'.

The symmetry of the circular aperture allows one to obtain the rms contribution of all speckle of the scalar spatial frequency corresponding to $\Delta q = |\Delta\mathbf{q}|$ with a simple integral over the direction θ,

$$\left\langle |C(\Delta q)|^2 \right\rangle = \int_0^{2\pi} \left\langle |C(\Delta\mathbf{q})|^2 \right\rangle \frac{\Delta q}{a^{1/2}}\, d\theta, \tag{27}$$

which gives

$$\left\langle |C(\Delta q)|^2 \right\rangle = \frac{8}{(\pi N)^{1/2}} \left(\frac{\Delta q}{2R}\right) \left[\cos^{-1}\left(\frac{\Delta q}{2R}\right) - \left(\frac{\Delta q}{2R}\right) \sqrt{1 - \left(\frac{\Delta q}{2R}\right)^2} \right]. \tag{28}$$

The argument $\Delta q/2R$ can be replaced by the equivalent expression

$$\frac{\Delta q}{2R} = \frac{K}{K_0}, \tag{29}$$

where the quantities not yet introduced are $K_0 = k_\nu / f$, the maximum spatial frequency present in the speckle modulation, and $f = z_0/2R$, the focal ratio or f number of the incident circular beam. The modulation spectrum from Eq. (28),

$$\left\langle |C(\Delta q)|^2 \right\rangle^{1/2},$$

is shown plotted in Fig. 68.19(a) as the "$\Delta\zeta/z_R = 0$" case. In this plot, the spectrum is normalized to give a peak value of unity, and the frequency variable is expressed in units of K_0 so that $\Delta q/2R = 1$ at full scale. This figure shows other results modified by axial averaging $(\Delta\zeta \neq 0)$, which will be explained in the following section. The speckle modulation results shown in Fig. 68.19 and in all subsequent figures are calculated for the case of the circular aperture.

The quantity $\left\langle |C(\Delta\mathbf{q})|^2 \right\rangle$ can be interpreted as the speckle power within an area ${k_\nu}^2\, a/{z_0}^2$ of the spatial frequency plane. This also represents the strength of the speckle modulation due to the interference between all DPP element pairs whose separations are given by all displacements within an area a centered about $\Delta\mathbf{q}$ on the $\mathbf{q}$ plane. The quantity $\left\langle |C(\Delta q)|^2 \right\rangle$, which has been integrated azimuthally, is to be interpreted as the speckle power within an interval $k_\nu\, a^{1/2}/z_0$ of spatial frequency $k_\nu\, \Delta q/z_0$. This is also the strength of the speckle modulation due to the interference between all DPP element pairs separated by all distances within a range $a^{1/2}$ of Δq.

Axial Averaging of the Speckle Spectrum

The time-averaged spatial distribution of the irradiation intensity at a surface within a plasma can be expressed as an axial average of the intensity distribution, as stated above. The results of the previous sections are now applied to the smoothing of speckle by axial averaging. The axial dependence of speckle modulation described by Eq. (21b) and ignored in the previous section is now considered. It will suffice for the present to consider simple uniform averaging over a range $\Delta\zeta$ of ζ,

$$\overline{C}(\Delta\mathbf{q}_m, \Delta\zeta) = \frac{1}{\Delta\zeta} \int_{-\Delta\zeta/2}^{\Delta\zeta/2} C(\Delta\mathbf{q}_m, \zeta)\, d\zeta. \tag{30}$$

This is appropriate if both the intensity and the plasma density are constant over this axial interval, such as when the time average is performed at a surface of constant electron density.

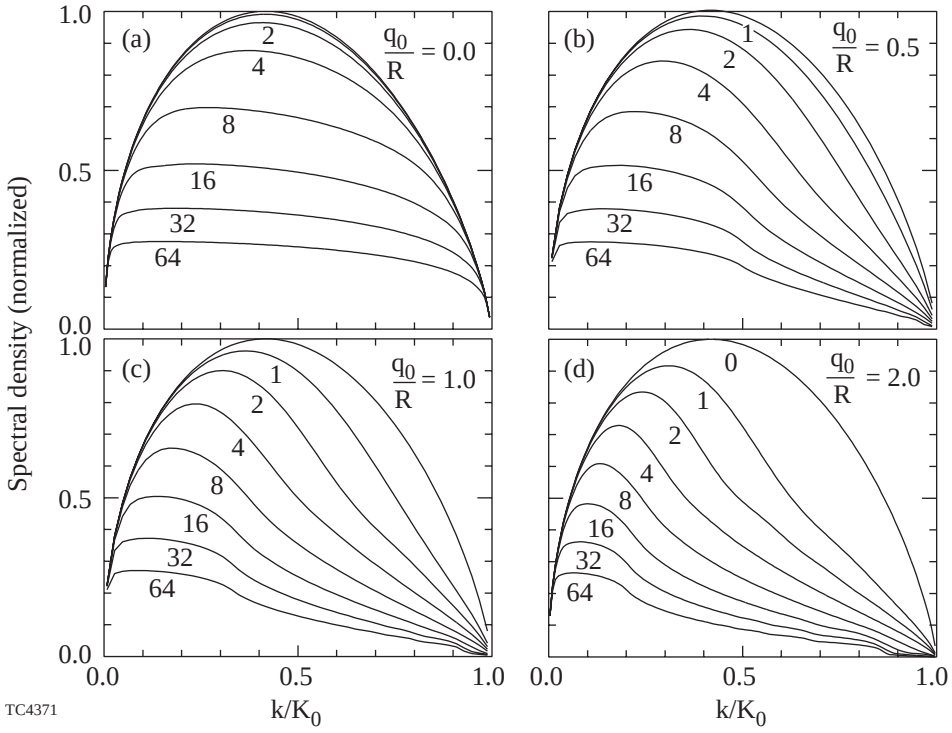

Figure 68.19
The spectral density of the speckle modulation factor, integrated over all directions of **K**, is plotted for various values of the smoothing distance, given in units of the Rayleigh range z_R. The spectral and frequency quantities are scaled to be plotted in units of their respective maximum values. Figure 68.19(a) shows results for normal incidence, $q_0/R = 0$. The unsmoothed spectrum is slightly asymmetric, and smoothing is only slightly more effective at higher frequencies. For the cases of non-normal incidence, $q_0/R =$ 0.5, 1.0, and 2.0, plotted in (b), (c), and (d), respectively, the smoothing effect is much stronger overall, particularly at higher frequencies.

In the case of an observer remaining at a fixed position so that $\Delta z = 0$ and where the local electron density remains constant, an evolving plasma atmosphere causes the value of ζ at that fixed point to change in time, resulting in a time average that is equivalent to an average over an interval of ζ. This simple average can also serve as a first-order estimate of results for cases where the weighting is not severely skewed due to absorption, intensity variability, or plasma inhomogeneity.

Applying Eq. (21b) to Eq. (30), the average obtained is

$$\overline{C}(\mathbf{\Delta q}_m,\Delta\zeta) = \frac{1}{N}\sum_{n=1}^{N_m}\frac{\sin\left[\dfrac{k_\nu\,\Delta\zeta}{2z_0^2}(\overline{\mathbf{q}}_n+\mathbf{q}_0)\cdot\mathbf{\Delta q}_m\right]}{\dfrac{k_\nu\,\Delta\zeta}{2z_0^2}(\overline{\mathbf{q}}_n+\mathbf{q}_0)\cdot\mathbf{\Delta q}_m}e^{-i\Delta\phi_{mn}}. \quad (31)$$

The expectation value of this sum is

$$\left\langle\left|\overline{C}(\mathbf{\Delta q}_m,\Delta\zeta)\right|^2\right\rangle = \frac{1}{N^2}\sum_{n=1}^{N_m}\frac{\sin^2\left[\dfrac{k_\nu\,\Delta\zeta}{2z_0^2}(\overline{\mathbf{q}}_n+\mathbf{q}_0)\cdot\mathbf{\Delta q}_m\right]}{\left[\dfrac{k_\nu\,\Delta\zeta}{2z_0^2}(\overline{\mathbf{q}}_n+\mathbf{q}_0)\cdot\mathbf{\Delta q}_m\right]^2}, \quad (32)$$

instead of Eq. (24). Just as Eq. (25) gives

$$\left\langle\left|C(\mathbf{\Delta q})\right|^2\right\rangle = \frac{1}{N^2}\iint\limits_{A\cap A'}\frac{d^2\overline{q}}{a} \quad (33)$$

as the large-N limit of Eq. (24), one obtains

$$\left\langle\left|\overline{C}(\mathbf{\Delta q},\Delta\zeta)\right|^2\right\rangle = \frac{1}{N^2}\iint\limits_{A\cap A'}\frac{\sin^2\left[\dfrac{k_\nu\,\Delta\zeta}{2z_0^2}(\overline{\mathbf{q}}+\mathbf{q}_0)\cdot\mathbf{\Delta q}\right]}{\left[\dfrac{k_\nu\,\Delta\zeta}{2z_0^2}(\overline{\mathbf{q}}+\mathbf{q}_0)\cdot\mathbf{\Delta q}\right]^2}\frac{d^2\overline{q}}{a} \quad (34a)$$

as the large-N limit of Eq. (32) for $\Delta\zeta \neq 0$. The same expression can be written

$$\left\langle\left|\overline{C}(\mathbf{\Delta q},\Delta\zeta)\right|^2\right\rangle = \frac{1}{N^2}\iint\limits_{A\cap A'}\frac{\sin^2\left[2\dfrac{\Delta\zeta}{z_R}\dfrac{(\overline{\mathbf{q}}+\mathbf{q}_0)}{R}\cdot\dfrac{\mathbf{\Delta q}}{2R}\right]}{\left[2\dfrac{\Delta\zeta}{z_R}\dfrac{(\overline{\mathbf{q}}+\mathbf{q}_0)}{R}\cdot\dfrac{\mathbf{\Delta q}}{2R}\right]^2}\frac{d^2\overline{q}}{a} \quad (34b)$$

for the case of the circular aperture, where the variables $\bar{\mathbf{q}}$ and $\mathbf{\Delta q}$ have been scaled in terms of the aperture radius R and where $\Delta\zeta$ has been scaled in terms of the Rayleigh range,[19]

$$z_R = \frac{8 f^2}{k_v} . \tag{35a}$$

This is the axial scale length of the intensity structure of a focused circular beam of focal ratio f and is the appropriate scale for measuring axial averaging distances. The magnitude of the oblique offset of the beam from normal incidence, $q_0 = |\mathbf{q}_0|$, is related to an angle of incidence ψ, where

$$\frac{q_0}{R} = 2 f \tan\psi . \tag{36a}$$

For small angles, $q_0 << 2 f R$, this gives

$$\psi \approx 4.09^\circ \frac{(q_0/R)}{(f/7)}, \tag{36b}$$

which shows that the sizable effects of oblique incidence expected with $q_0 \sim R$ are obtained with small angles of incidence.

Figure 68.19 shows several normalized speckle spectra,

$$\left\langle \left| \bar{C}(\Delta q, \Delta\zeta) \right|^2 \right\rangle^{1/2},$$

plotted as functions of spatial frequency K, written in units of $K_0 = k_v / f$, the maximum spatial frequency present in the speckle modulation. The quantities $\mathbf{K}$ and $\mathbf{\Delta q}$ are related by Eq. (23). These results have been obtained by evaluating Eq. (34b) numerically to obtain $\left\langle \left| \bar{C}(\mathbf{\Delta q}, \Delta\zeta) \right|^2 \right\rangle$, which is then averaged numerically over all directions of $\mathbf{K}$. Figure 68.19(a) shows results for normal incidence, $q_0/R = 0$. Each curve represents a different degree of axial averaging and is labeled by the smoothing interval $\Delta\zeta/z_R$, expressed in units of the Rayleigh range z_R. It is seen that values of $\Delta\zeta$ of the order of several z_R are needed for significant smoothing. The cases of nonnormal incidence, $q_0/R = 0.5$, 1.0, and 2.0, are plotted in Figs. 68.19(b), 68.19(c), and 68.19(d), respectively. These results show that the smoothing effect is enhanced significantly by only a slight tilt of the beam, particularly at higher spatial frequencies. According to Eqs. (36), the $q_0/R = 2.0$ case, for example, represents an angle of incidence of only 8.2° for a focal ratio of f/7.

Since higher transverse speckle frequencies correspond to stronger axial dependence, it would be expected that the smoothing for a given $\Delta\zeta$ would be strongest at higher speckle frequencies, but the $q_0/R = 0$ case plotted in Fig. 68.19(a) shows an averaging effect that is surprisingly symmetric about the middle speckle frequencies where it is strongest, in contrast to the highest and lowest frequencies where it is weakest. The least smoothing is expected at the lowest frequencies since this modulation is due to the interference of ray pairs that are closest in angle and thus produce interference structure with the weakest axial and transverse dependence. The high-frequency components, on the other hand, are dominated by interfering wave pairs that cross at the largest angles. This should lead to strong axial dependence, but the ray pairs with the largest crossing angles all originate from nearly opposite positions near the rim of the aperture at nearly opposite angles from the beam axis. In this limit, the interference patterns lack spatial dependence along the axis of the beam. Consequently, axial averaging has a vanishing effect at the highest speckle frequencies. Away from normal incidence, the symmetry axes of the beam and the plasma profile no longer coincide, and spatial averaging along the z axis does reduce the speckle modulation at the highest frequencies.

The spectral information plotted in Fig. 68.19 is recast in Fig. 68.20 as sets of curves, each representing the spatial frequency indicated by its label and each plotted as a function of the axial averaging distance. As in previous figures, the spatial frequency is written in units of the maximum frequency $K_0 = k_v / f$, and the averaging distance is expressed in units of the Rayleigh range z_R. The case of normal incidence is shown in Fig. 68.20(a), and the cases of nonnormal incidence, $q_0/R = 0.5$, 1.0, and 2.0, are shown in Figs. 68.20(b), 68.20(c), and 68.20(d), respectively. The $(\Delta\zeta)^{-1/2}$ scaling of the smoothing effect is seen clearly for large $\Delta\zeta/z_R$. Figure 68.20(e) summarizes these results with a set of curves, each representing the rms spectral average of the speckle modulation spectrum obtained for a given angle of incidence, plotted as functions of the averaging interval $\Delta\zeta/z_R$. Each curve is labeled by the assumed value of q_0/R.

The spectral information plotted in Fig. 68.19 is also recast in Fig. 68.21, where Figs. 68.21(a), 68.21(b), and 68.21(c) show sets of curves obtained for axial smoothing distances $\Delta\zeta/z_R =$ 2.0, 4.0, and 8.0, respectively, now plotted as functions of the incidence parameter of q_0/R. Each curve represents the spatial frequency indicated by its label, and each curve is plotted as a function of the angle of incidence, represented in the plot by the oblique offset q_0/R. As in

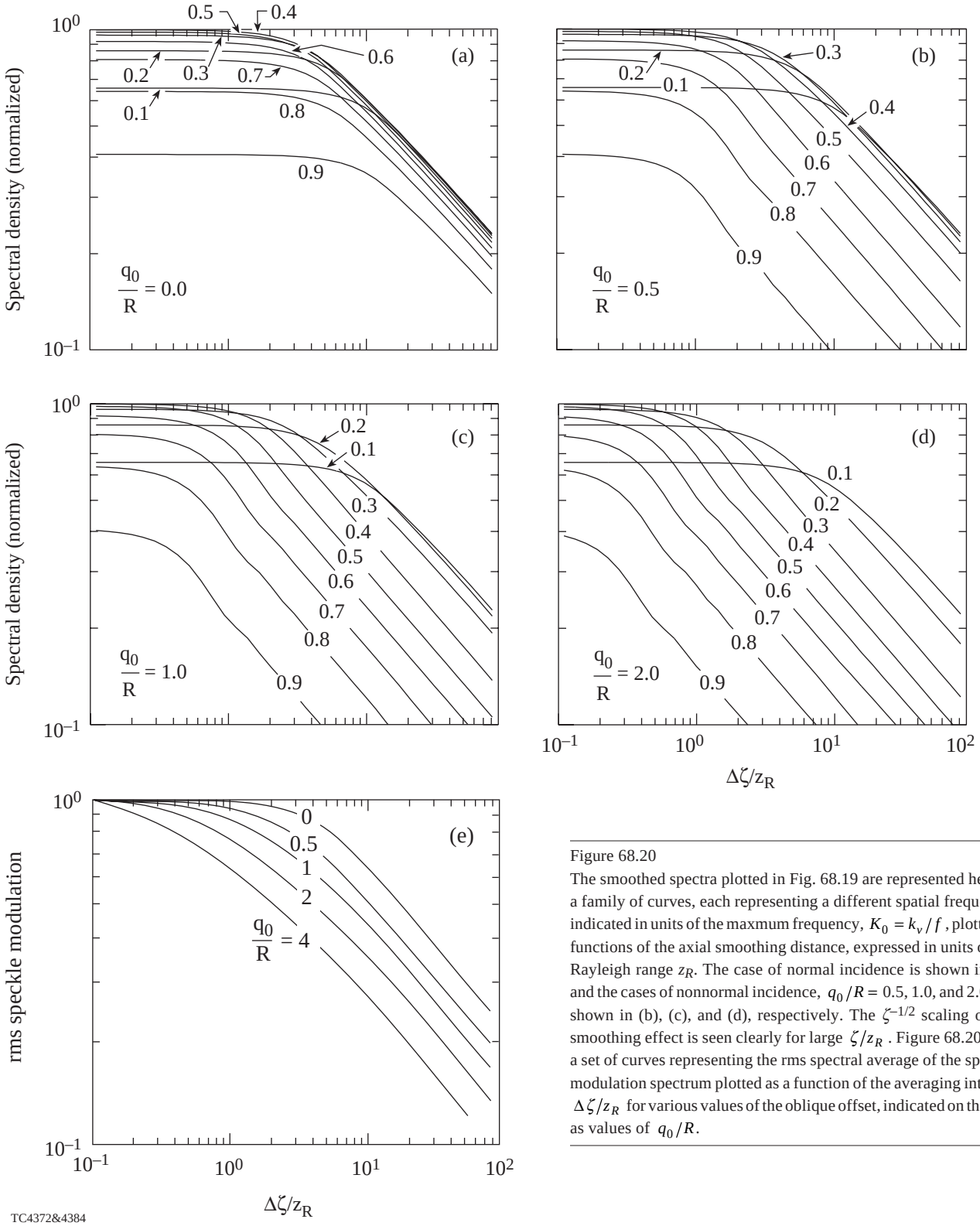

Figure 68.20

The smoothed spectra plotted in Fig. 68.19 are represented here as a family of curves, each representing a different spatial frequency, indicated in units of the maxmum frequency, $K_0 = k_v / f$, plotted as functions of the axial smoothing distance, expressed in units of the Rayleigh range z_R. The case of normal incidence is shown in (a), and the cases of nonnormal incidence, $q_0 / R = 0.5$, 1.0, and 2.0, are shown in (b), (c), and (d), respectively. The $\zeta^{-1/2}$ scaling of the smoothing effect is seen clearly for large ζ / z_R. Figure 68.20(e) is a set of curves representing the rms spectral average of the speckle modulation spectrum plotted as a function of the averaging interval $\Delta\zeta / z_R$ for various values of the oblique offset, indicated on the plot as values of q_0 / R.

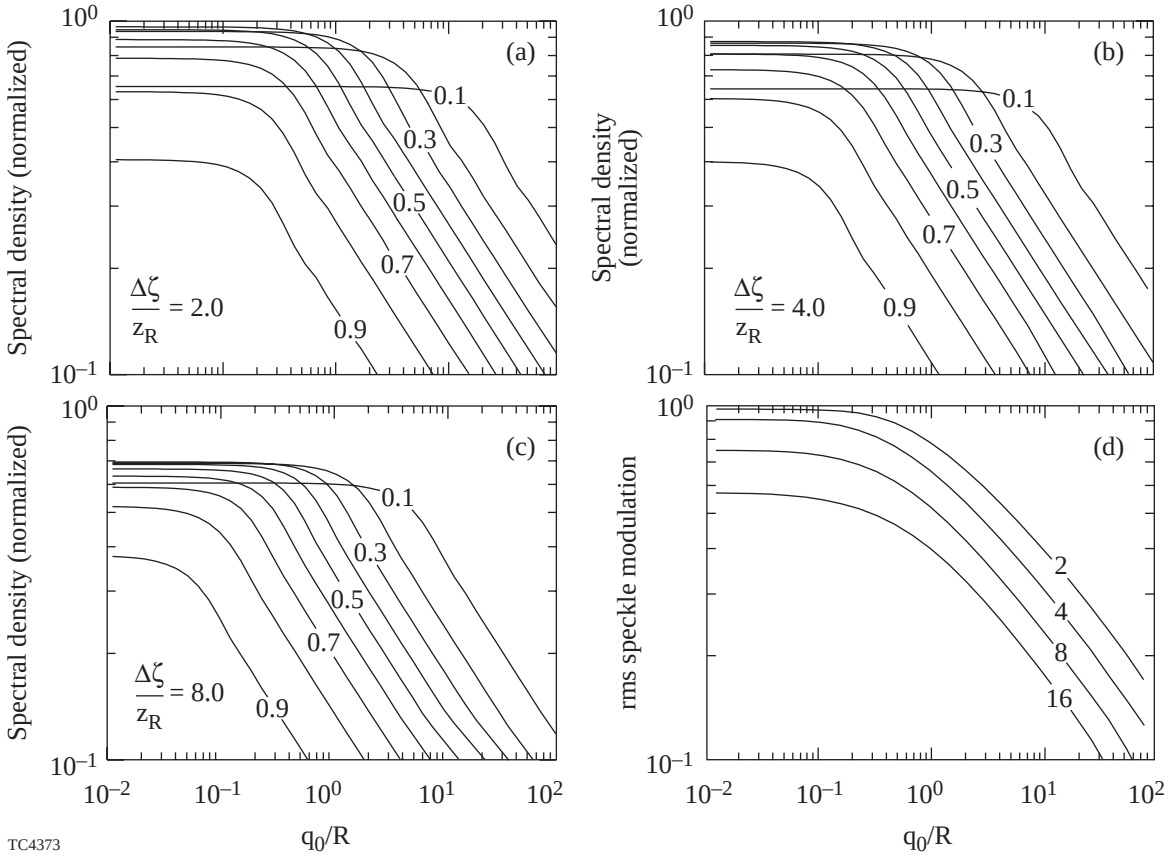

Figure 68.21
The smoothing of the spectra plotted in Fig. 68.19 is represented here as a family of curves, each representing a different spatial frequency indicated in units of the maximum frequency, $K_0 = k_\nu / f$, plotted as functions of the oblique offset, represented in units of q_0/R, for values of the axial smoothing distance $\Delta\zeta/z_R =$ 2.0, 4.0, and 8.0, in (a), (b), and (c), respectively. The curves are carried out to large values of q_0/R in order to show more clearly the $(q_0/R)^{-1/2}$ scaling of the smoothing effect, even though the paraxial approximation is violated for values of q_0/R that are not small compared to the focal ratio. Figure 68.21(d) is a set of curves representing the rms spectral average of the speckle modulation spectrum plotted as a function of oblique offset for various smoothing distances indicated on the plot as values of $\Delta\zeta/z_R$.

previous figures, the spatial frequency is written in units of the maximum frequency $K_0 = k_\nu / f$. The curves are carried out to large values of q_0/R for the sole purpose of highlighting the $(q_0/R)^{-1/2}$ scaling of the axial-averaging effect. It must be remembered that the paraxial approximation is valid only for values of q_0/R that are small compared to the focal ratio *f*. Figure 68.21(d) summarizes these results with a set of curves, each representing the rms spectral average of the speckle modulation spectrum obtained for a given axial-averaging interval, plotted as a function of the oblique offset q_0/R. Each curve is labeled by the assumed value of $\Delta\zeta/z_R$.

Figures 68.20(e) and 68.21(d) show what size axial-averaging interval $\Delta\zeta/z_R$ and oblique offset q_0/R are needed for a given reduction in the rms speckle modulation. For the purposes of this discussion, a factor of 2 will be taken as the nominal desired smoothing factor. At normal incidence, an axial-averaging interval of about 20.0 z_R is needed for this amount of smoothing. This is about one order of magnitude greater than expected, given that the Rayleigh range z_R is the characteristic length of the axial dependence of the speckle distribution. This surprising result is due to a surprising degree of axial independence in the speckle distribution along the beam axis. At only a modest angle of incidence, however, the same amount of smoothing is obtained with a much shorter axial-averaging interval. Oblique displacements of $q_0/R = 0.5$, 1.0, 2.0, and 4.0 reduce the axial-averaging interval to approximately $\Delta\zeta/z_R = 10.0$, 7.0, 4.0, and 2.0, respectively. An

approximate scaling relationship for the oblique displacements and averaging intervals needed to obtain a smoothing reduction factor r can be inferred from the asymptotic behavior seen in Figs. 68.20 and 68.21 and from the above $\Delta\zeta/z_R$ and q_0/R values found to produce a speckle reduction factor of 0.5:

$$r^2 \approx 2.5\left(\frac{\mathbf{q}_0}{R}+0.5\right)^{-1}\left(\frac{\Delta\zeta}{z_R}\right)^{-1}. \qquad (37a)$$

Since this expression has been fit to results that are not well into the scaling regimes of $\Delta\zeta/z_R$ and, in particular, q_0/R, this expression must be applied with caution as no more than a guide for the parameter ranges under consideration.

For the purposes of the discussion to follow, the range of $\Delta\zeta/z_R$ from 2 to 4 will be taken as a guide to what amount of axial averaging suffices for a significant amount of smoothing. This gives a factor-of-0.5 reduction in the rms speckle modulation for oblique displacements q_0/R in the approximate range from 4 to 2. As was mentioned above, this range corresponds to very modest angles of incidence, about 16° at most for *f*/7 irradiance. For multiple-beam experiments, angles of incidence of this order cannot be avoided. The absolute minimum oblique offset of $q_0/R = 1$ is obtained for the case of two beams whose focus lenses are touching. For a closely packed cluster of six beams in a hexagonal array, $q_0/R = 2$ is the absolute minimum. Allowing the beam edges to come no closer than one beam diameter doubles this to $q_0/R = 4$.

Thus far, all calculations and results have been expressed in terms of the oblique offset q_0/R and the Rayleigh range z_R because these are the parameters most characteristic of the speckle structure and the smoothing requirements. In describing an experimental configuration, the angle of incidence is more meaningful than q_0/R. The Rayleigh range given by Eq. (35a) written in terms of fundamental units is

$$z_R = 22\,\mu\text{m}\left(\frac{\lambda_v}{0.351\,\mu\text{m}}\right)\left(\frac{f}{7}\right)^2. \qquad (35b)$$

The potential of an atmosphere for smoothing speckle is in large part a function of its scale length in units of z_R. One is reminded by Eq. (35b) that this figure of merit is a function of the laser wavelength λ_v and the focal ratio *f*. Equations (35b) and (36b) inserted into Eq. (37a) give

$$r^2 \approx 2.5\frac{\left(\frac{\lambda_v}{0.351\,\mu\text{m}}\right)\left(\frac{f}{7}\right)}{\left(\frac{\psi}{4.1°}\right)\left(\frac{\Delta\zeta}{22\,\mu\text{m}}\right)} \qquad (37b)$$

as an estimate of the speckle-reduction factor r expected from an angle of incidence ψ and an axial-averaging interval $\Delta\zeta$. This expression has been simplified by assuming that $q_0/R > 1.0$ is amply satisfied as if the speckle smoothing were in the $(q_0/R)^{-1/2}$ scaling regime, as seen in Fig. 68.21. An important conclusion to be drawn from Eq. (37b) is that the axial-averaging length $\Delta\zeta$ required to produce a given smoothing is proportional to the focal ratio f when the angle of incidence is within its scaling regime. This is a more-favorable focal-ratio scaling than is obtained near normal incidence when the smoothing is a function of $\Delta\zeta/z_R$ alone. In that case, Eqs. (35b) and (37a) show that the required $\Delta\zeta$ scales as the square of the focal ratio f for a specified value of r.

The smoothing of speckle by axial averaging and by SSD or ISI ought to have similar asymptotic time dependence since both work by the uniform averaging in time of the same random quantity. As long as $\Delta\zeta$ increases uniformly in time, the $\Delta\zeta^{-1/2}$ scaling of the axial smoothing factor corresponds to $(\Delta\nu\, t)^{-1/2}$, which is the reduction factor due to SSD and ISI at late times, where $\Delta\nu$ is the bandwidth of the laser output.[20] These identical time dependences allow the axial-averaging reduction factor to be written in terms of an effective bandwidth as well. The effectiveness of smoothing by axial averaging can thus be readily compared with that of SSD and ISI by comparing bandwidths.

The next two sections consider circumstances under which laser ablation of a target can produce an adequate axial-averaging interval and how fast this averaging can occur.

The Plasma Effect

In this section the plasma effect alone is considered. The time average of the speckle is calculated at an absorption plane that is kept fixed in space, relative to the laser, while the plasma profile in the beam path changes in time. The magnitude of this effect is evaluated below for the case of an expanding plane-parallel atmosphere. The case of a spherically diverging plasma is also considered briefly because even in an experiment using a planar target, the plasma atmosphere does approach a spherically diverging profile beyond a distance comparable to the diameter of the illumination spot. This comparison of the plasma shift of the speckle for both a spherical and a plane-

parallel case clarifies this limitation of the plane-parallel assumption applied to the irradiation of a planar target. A more complete analysis of speckle averaging due to both the plasma and hydrodynamic effects is done in the following section entirely in terms of the plane-parallel, isothermally expanding atmosphere model.

An example of an expanding plane-parallel plasma profile is the exponential density profile that is obtained for the case of isothermal rarefaction,[6,21] which is considered in more detail in the **Discussion** section. For the simplest case of full, constant ionization, where the electron and mass densities are in a fixed ratio, the electron density can be written as

$$\frac{n_e(z)}{n_{\text{abs}}} = e^{-(z-z_{\text{abs}})/L}, \tag{38}$$

where n_{abs} is the electron density at the absorption surface, a constant-density surface fixed for now at $z = z_{\text{abs}}$. The laser enters the plasma from the $+z$ direction, and the scale length L grows in time as ablation fills the atmosphere with plasma. The on-target intensity uniformity is to be determined at the absorption surface. An expression for ζ_p, the plasma contribution to the axial distance parameter obtained from Eq. (9), is

$$\frac{\zeta_p(z_{\text{abs}})}{z_R} = \frac{k_v}{8f^2}\int_{z_{\text{abs}}}^{\infty}\left(\frac{1}{\sqrt{1-n_e/n_c}}-1\right)dz'. \tag{39}$$

Using Eq. (38), this gives

$$\frac{\zeta_p(z_{\text{abs}})}{z_R} = \frac{k_v L}{4f^2}\ln\left[\frac{2}{1+\left(1-n_{\text{abs}}/n_c\right)^{1/2}}\right], \tag{40}$$

which gives $\Delta\zeta_p$, the change in ζ_p due to the growth of the atmosphere by an increment ΔL,

$$\frac{\Delta\zeta_p}{z_R} = \frac{k_v \Delta L}{4f^2}\ln\left[\frac{2}{1+\left(1-n_{\text{abs}}/n_c\right)^{1/2}}\right]. \tag{41}$$

The quantity $\Delta\zeta_p$ is the averaging interval to be used to calculate the time averaging that occurs over the interval of time that the atmosphere grows by an increment ΔL.

The averaging effect described by Eq. (41) grows with increasing n_{abs}/n_c. The limit $n_{\text{abs}} \to n_c$ gives an indication of the maximum effect obtainable, although the restriction imposed on n_{abs}/n_c by Eqs. (14) must be applied case-by-case to ensure consistency with the paraxial approximation. Using parameter values typical of ICF, this limit is

$$\frac{\Delta\zeta_{p\max}}{z_R} = 6.33\frac{(\Delta L/100\,\mu\text{m})}{(\lambda_v/0.351\,\mu\text{m})(f/7)^2}, \tag{42a}$$

for the axial-averaging parameter applicable to the time interval during which the atmosphere expands by ΔL. In this idealized plasma model, a given increase in L is equivalent to an increase in the mass per unit area of the atmosphere exterior to the absorption surface. This mass per unit area is equivalent to a certain thickness of target material at its original density. For a solid CH polymer with a solid density of 1 g/cm^3, the averaging interval resulting from turning a thickness Δr_{CH} of target material into fully ionized atmospheric plasma is

$$\frac{\Delta\zeta_{p\max}}{z_R} = 4.72\frac{(\Delta r_{\text{CH}}/2\,\mu\text{m})}{(\lambda_v/0.351\,\mu\text{m})(f/7)^2}. \tag{42b}$$

This shows that an ICF plasma can shift the speckle intensity distribution by a significant amount, but that a substantial thickness of material, roughly the equivalent of a few microns of polymer, must be ablated. Even though an ICF plasma introduces enough phase dispersion and refraction to shift the speckle pattern by amounts needed for significant reduction by averaging, whether or not this provides a useful averaging rate depends on how fast the atmosphere grows and on whether or not a useful degree of averaging occurs before an irreversible imprint of the instantaneous nonuniformity has had time to develop. The likelihood of this being achieved in planar ablation experiments is the subject of the following section.

The most important consequence of spherical divergence is that the plasma effect is limited by the flow geometry. The plasma effect due to a planar atmosphere, on the other hand, is limited only by the supply of ablated plasma, or from the point of view of Eq. (40), ζ_p grows as long as L continues to grow. In the case of a finite illumination spot on a planar target, the atmosphere approaches spherical divergence with increasing distance from the target, and the upper limit on ζ_p depends on many things, including how quickly the transition from planar to spherical expansion occurs with increasing distance from the illumination spot, but a finite limit does exist. To show that spherical divergence results in a finite limit, even for an infinite atmosphere, it suffices to consider the density profile given by

Eq. (38), modified for late times by taking the limit $L \to \infty$ and modified for spherical divergence at all radii with appropriate radial scaling. The result is

$$n_e = n_{\text{abs}} \left(\frac{r_{\text{abs}}}{r} \right)^2 , \tag{43}$$

where the absorption surface is located at the radius $r = r_{\text{abs}}$. The maximum plasma contribution to the axial distance parameter for this case, $\zeta_{p\,\max}$, is obtained by evaluating Eq. (9), which gives

$$\frac{\zeta_{p\max}(r_{\text{abs}})}{z_R} = \frac{k_v\, r_{\text{abs}}}{8\, f^2} \left[1 - \left(1 - n_{\text{abs}}/n_c \right)^{1/2} \right]. \tag{44}$$

This expression resembles Eq. (40) closely, except that the radius of the absorption surface r_{abs} has replaced the scale length L as the characteristic length of the problem. The dependences on n_{abs}/n_c are qualitatively similar. Equation (44) can be written in practical units as

$$\frac{\zeta_{p\max}(r_{\text{abs}})}{z_R} = 22.8 \frac{\left(\dfrac{r_{\text{abs}}}{500\,\mu\text{m}} \right)}{\left(\dfrac{\lambda_v}{0.351\,\mu\text{m}} \right) \left(\dfrac{f}{7} \right)^2} \left[1 - \left(1 - n_{\text{abs}}/n_c \right)^{1/2} \right]. \tag{45}$$

The maximum axial-averaging interval that can occur, given these nominal parameter values and absorption at the critical surface $\left(n_{\text{abs}} = n_c \right)$, is 22.8 z_R. As before, Eqs. (14) restrict n_{abs} to values consistent with the paraxial approximation, and smaller intervals are obtained for absorption at less than critical density. Equation (44) describes a case where the ablative flow is completely spherical from the absorption surface outward. It does not apply directly to the case where the ablative flow makes a transition from planar flow near the absorption surface to spherical flow at large distances from the target, but it does show that spherical divergence does prevent the axial-averaging interval from growing without limit. This means that a planar model must be applied with caution to cases where a significant contribution to $\zeta_p(z)$ is due to plasma that is diverging from plane-parallel flow.

The Combined Plasma and Hydrodynamic Effects

The motion of the absorption surface relative to the irradiation-intensity distribution is due to both the hydrodynamic motion of the absorption surface and the accumulation of plasma in the propagation path. The essential behavior of these effects and their relative importance can be described and understood by applying Eq. (9) to a planar 1-D isothermal rarefaction model for steady-state ablation of a planar target. At the beginning of the irradiation, when the target is vulnerable to being irreversibly imprinted with the laser nonuniformity, the solid target surface is at rest, and the absorption surface is being convected away from the solid target surface by the expanding atmosphere. At this time, the plasma effect is moving the intensity distribution toward the laser, in the same direction as the motion of the absorption surface, so the hydrodynamic and plasma effects tend to cancel each other. The hydrodynamic effect starts out roughly a factor of 2 faster than the plasma effect. As the target accelerates away from the laser, the hydrodynamic effect begins to reverse, and the plasma and hydrodynamic effects eventually reinforce each other.

In the planar 1-D isothermal rarefaction model, the mass-density profile is of the form of Eq. (38).[21] The growth rate of scale length L is the fluid velocity at the ablation source point at the target's surface, which will be identified below as the isothermal sound speed c_T. Assuming a constant, fixed ionization state, this gives

$$\frac{n_e(z)}{n_s} = \exp\left\{ -\left[\frac{z - z_s(t)}{c_T t} \right] \right\}, \tag{46}$$

where the substitution

$$L = c_T\, t \tag{47}$$

has been made, where n_s is the electron density of the ablated plasma at the source point, and where $z_s(t)$ is the position of the source point at the solid surface. It is assumed that the target motion remains much slower than c_T so that Eq. (46) remains an adequate description of the plasma atmosphere between the target surface and the absorption region, independent of the target's motion.

Given a mass-density profile of the form of Eq. (46), conservation of mass

$$\frac{\partial \rho}{\partial t} + \frac{\partial}{\partial z}(\rho v) = 0 \tag{48}$$

dictates

$$v(z,t) = c_T + \frac{z - z_s(t)}{t}, \tag{49}$$

and the momentum equation

$$\frac{\partial v}{\partial t} + v\frac{\partial v}{\partial z} + \frac{1}{\rho}\frac{\partial P}{\partial z} = 0 \tag{50}$$

is satisfied by the isothermal equation of state

$$P = c_T^2\,\rho, \tag{51}$$

where the identification of c_T with the isothermal sound speed is now clear.

The motion of the solid target is obtained by treating it as a planar rocket accelerated by the ablating plasma. Its mass per unit area, M, decreases at a rate determined by the plasma density ρ_s and plasma velocity $v(z_s,t) = c_T$ at the ablation source point,

$$M = M_0 - \rho_s c_T t. \tag{52}$$

The force accelerating the remaining solid target is equal to the rate at which momentum is imparted to the ablation exhaust, which gives

$$M\frac{dV}{dt} = -\rho_s\, c_T^2, \tag{53}$$

and the solution

$$V = c_T \ln\left(1 - \frac{\rho_s\, c_T\, t}{M_0}\right) \tag{54}$$

for velocity V of the remaining solid target. This solution gives a velocity that accelerates smoothly from rest, so the motion of the solid target does not contribute to the motion of the absorption surface at the very beginning of the ablation, $t << M_0/\rho_s c_T$, when the most significant imprinting of the laser nonuniformity occurs.

In estimating the effects of ablation on uniformity, it is assumed here that the absorption of laser energy occurs over a sufficiently short range that one can speak of an absorption surface at a point of fixed density where the irradiation nonuniformity has its effect on the plasma. The absorption surface is identified by the local mass density ρ_{abs}. According to Eq. (46), this absorption surface is positioned ahead of the ablation source by a distance z_{abs} given by

$$z_{\text{abs}} = c_T\, t \ln\left(\frac{\rho_s}{\rho_{\text{abs}}}\right). \tag{55}$$

This contribution to the motion of the absorption surface is a constant velocity with respect to the target surface and is the main contribution to the averaging rate at early times. The total motion of the absorption surface, written as the hydrodynamic contribution to the rate of increase of the smoothing distance, $\Delta\zeta$, is

$$\frac{1}{c_T}\frac{d\Delta\zeta_h}{dt} = -\ln\left(1 - \frac{\rho_s\, c_T\, t}{M_0}\right) - \ln\left(\frac{\rho_s}{\rho_{\text{abs}}}\right). \tag{56}$$

The total effect is obtained by adding to this the plasma contribution to $\Delta\zeta_p$ given by Eq. (41), which gives

$$\frac{1}{c_T}\frac{d\Delta\zeta}{dt} = -\ln\left(1 - \frac{\rho_s\, c_T\, t}{M_0}\right) - \ln\left(\frac{\rho_s}{\rho_{\text{abs}}}\right) + 2\ln\left[\frac{2}{1+\left(1-n_{\text{abs}}/n_c\right)^{1/2}}\right]. \tag{57}$$

This expression can be written entirely in terms of the absorption density as a fraction of the critical density by relating the critical electron density to the solid density of the target ρ_{solid},

$$\frac{\rho_s}{\rho_{\text{abs}}} = 38.8\left(\frac{\rho_{\text{solid}}}{1\,\text{g}\cdot\text{cm}^{-3}}\right)\left(\frac{\lambda_v}{0.351\,\mu\text{m}}\right)^2\left(\frac{Z}{3.5}\right)\frac{\rho_s}{\rho_{\text{solid}}}\frac{n_c}{n_{\text{abs}}}. \tag{58}$$

The quantities in parentheses are chosen to be unity, which represents fully ionized CH polymer. Equation (57) can now be written as

$$\frac{1}{c_T}\frac{d\Delta\zeta}{dt} = -3.66 - \ln\left[\left(\frac{\rho_{\text{solid}}}{1\,\text{g}\cdot\text{cm}^{-3}}\right)\left(\frac{\lambda_v}{0.351\,\mu\text{m}}\right)^2\left(\frac{Z}{3.5}\right)\right] - \ln\left(1 - \frac{\rho_s\, c_T\, t}{M_0}\right) - \ln\left(\frac{\rho_s}{\rho_{\text{solid}}}\right) + 2\ln\left[\frac{2\left(n_{abs}/n_c\right)^{1/2}}{1+\left(1-n_{\text{abs}}/n_c\right)^{1/2}}\right]. \tag{59}$$

The first two terms contain only parameters that are fixed by the choice of target and laser, including the density of the cold target material, ρ_{solid}, the laser wavelength λ_v, and a fixed ionization state Z. The third term represents the acceleration part of the hydrodynamic effect, which depends on the initial areal mass of the target M_0 and vanishes in the early-time, $L = 0$ limit. The remaining terms depend only on ρ_s as a fraction of the solid density and n_{abs} as a fraction of the critical density.

Hydrodynamic simulations of the ablation and acceleration of a CH polymer slab by a constant irradiance have been performed using the 1-D hydrocode *LILAC*. The hydrodynamic and plasma contributions to $\Delta\zeta/z_R$ and the total effect are evaluated from these results and plotted as functions of time in Fig. 68.22. The absorption surface is taken to be the centroid of the energy-absorption rate distribution. The hydrodynamic and plasma effects are obtained from the geometric and plasma contributions to the integral in Eq. (9), respectively, which is evaluated from the position of the absorption surface and from the electron-density profile given by the simulation. The solid curves in Figs. 68.22(a), 68.22(b), and 68.22(c) are results obtained from simulations of the ablation of a planar target irradiated by 10^{13}, 10^{14}, and 10^{15} W/cm^2 UV ($\lambda_v = 0.351$ μm), respectively. The target is a CH polymer foil 10 μm thick and 1.0 g/cm^3 in density.

The isothermal-expansion rocket model described above and given by Eq. (59) is fit to the results of the hydrodynamic simulations, including those in Fig. 68.22. The fitted model results are shown in Fig. 68.22 as dashed curves, which accomplishes two things: First, it is seen that the fit is reasonably good over the entire range of intensities, which validates the isothermal expansion model as a basis for describing and deriving preliminary general statements about the effects that lead to axial averaging of speckle over time. Second, the isothermal rocket model serves as a template that can be fit to the simulation results to obtain appropriate values of model parameters and average smoothing rates from the simulations. The separate plasma and hydrodynamic contributions to the total smoothing rate at the very beginning of the irradiation pulse, and the total smoothing rate at that time, were obtained from these fits and plotted as functions of intensity in Fig. 68.23.

The results shown in Figs. 68.22 and 68.23 clearly show that the initial smoothing effect is greatly diminished by the fact that the hydrodynamic and plasma effects counteract each other. These results show that the total initial smoothing rate varies between about 1.5 and 3 Rayleigh lengths per nanosecond over the range of intensities from 10^{13} W/cm^2 to 10^{15} W/cm^2, where the Rayleigh length is the 22-μm value obtained for the nominal parameter values from Eq. (35b).

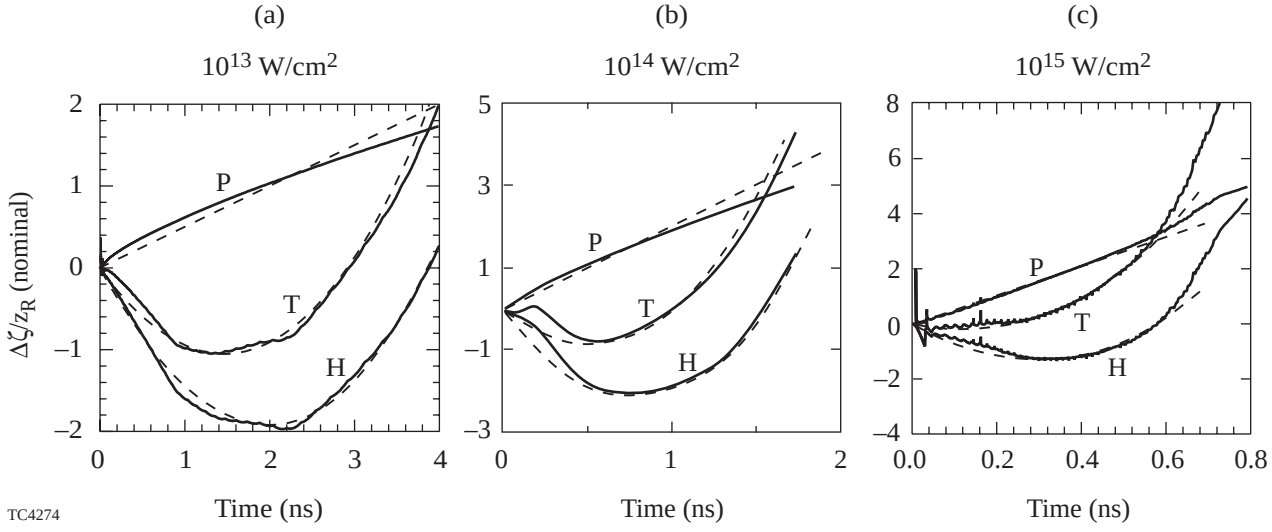

Figure 68.22
The hydrodynamic and plasma contributions to $\Delta\zeta/z_R$ and the total effect are plotted as functions of time. Solid curves are results obtained from numerical simulations of the ablation of a planar target irradiated by 10^{13}, 10^{14}, and 10^{15} W/cm^2 UV ($\lambda_v = 0.351$ μm) in (a), (b), and (c), respectively. The dashed curves are fits of a simple rocket model of planar ablation based on the isothermal expansion of the atmosphere. The value of z_R here is 22 μm, which is obtained from Eq. (35b) for the nominal parameter values.

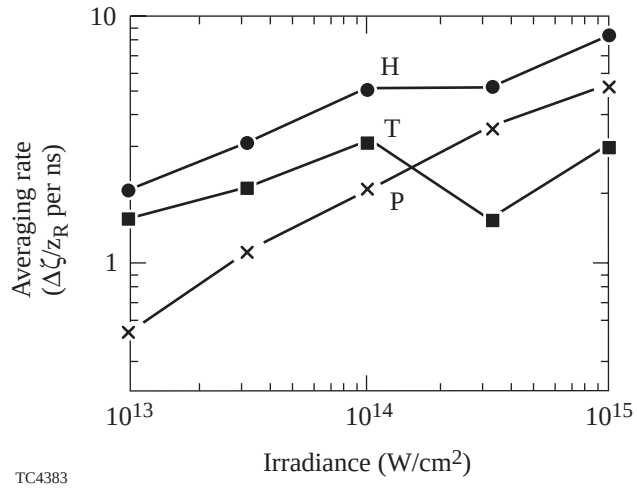

Figure 68.23
The plasma (*P*) and hydrodynamic (*H*) contributions to the smoothing rate $1/z_R\ d\Delta\zeta/dt$ and total effect (*T*) are plotted versus intensity.

Given that the range of required $\Delta\zeta/z_R$ values varies from 2 to 4, as was stated earlier, the range of smoothing times varies from 0.67 ns to 2.67 ns. These smoothing times are comparable to hydrodynamic time scales typical of ICF experiments, but they are longer than other important scale times, such as the time during which the initial nonuniformity of the laser beam is irreversibly imprinted onto the target and the time scale of self-focusing. Averaging as slow as this clearly would not suffice as the sole smoothing mechanism in ICF, but this is not a negligible effect, and it could have an important quantitative significance on certain experimental results where DPP's are used without SSD, such as when measuring the effects of SSD on the outcome of ICF experiments. Of course, variations in focus, wavelength, laser configuration, target geometry, target composition, etc., can give averaging times that vary significantly from these estimates.

To create a situation where the hydrodynamic and plasma effects reinforce each other, a set of numerical simulations was done with a target identical to the 10-μm foil used in the simulations in Figs. 68.22 and 68.23, except that the outermost 2.5 μm of solid CH polymer has been changed to an equal areal mass of 50-μm-thick foam. The hydrodynamic and plasma contributions to $\Delta\zeta/z_R$ and the total effect are plotted in Fig. 68.24(a) as functions of time for the ablation of this target under an irradiation intensity of 10^{14} W/cm^2 UV (λ_v = 0.351 μm), to compare with Fig. 68.22(b). With the foam layer in place, the absorption surface moves away from the laser initially, and the plasma and hydrodynamic effects reinforce each other. The plasma and hydrodynamic contributions to the initial smoothing rate $1/z_R\ d\Delta\zeta/dt$ and the total initial effect are plotted as functions of intensity in Fig. 68.24(b). The isothermal rocket model applied to the homogeneous slab targets is not applicable to this more complicated target, so these rates are estimates obtained by eye. The total smoothing rate is now between about 2.0 and 20.0 Rayleigh lengths per nanosecond over the range of intensities from 10^{13} W/cm^2 to 10^{15} W/cm^2, which corresponds to smoothing times of from

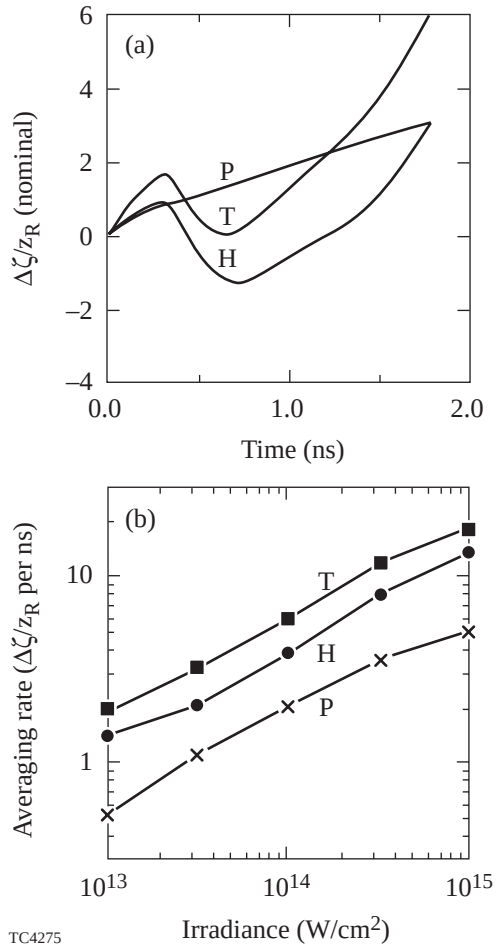

Figure 68.24
The hydrodynamic (*H*) and plasma (*P*) contributions to $\Delta\zeta/z_R$ and the total effect (*T*) obtained from a numerical simulation are plotted in Fig. 68.24(a) as functions of time for the case of the ablation of a planar target irradiated by 10^{14} W/cm^2 UV (λ_v = 0.351 μm). The target is identical to the 10-μm foil used in the simulations shown in Fig. 68.22, except that the outermost 2.5 μm of solid CH polymer has been changed to an equal mass of foam 50 μm thick. In this case, the absorption surface moves away from the laser, and the plasma and hydrodynamic effects reinforce each other. The plasma and hydrodynamic contributions to the initial smoothing rate $1/z_R\ d\Delta\zeta/dt$ and the total effect are plotted versus intensity in Fig. 68.24(b). The value of z_R is 22 μm, which is obtained from Eq. (35b) for the nominal parameter values.

100 ps to 2.0 ns, up to more than an order of magnitude faster than is obtained with a solid target.

As stated above, the $(\Delta\nu\, t)^{-1/2}$ asymptotic time dependence of the smoothing effect of SSD and ISI corresponds identically to the $\Delta\zeta^{-1/2}$ asymptotic dependence of the speckle reduction on the averaging interval. When the axial-averaging rate $d\Delta\zeta/dt$ is a constant, an effective bandwidth $\Delta\nu_{\text{axial}}$ can be written for axial averaging and compared with the bandwidth $\Delta\nu_{\text{SSD}}$ specified for an SSD system. Recalling Eq. (37a) and making the identification $r^{-2} = \Delta\nu_{\text{axial}}\, t$, one obtains

$$\Delta\nu_{\text{axial}} = 0.4\,\text{GHz}\left(\frac{\mathbf{q}_0}{R} + 0.5\right)\left(\frac{1}{z_R}\frac{d\Delta\zeta}{dt}\right). \qquad (60)$$

Recalling the $1/z_R\ d\Delta\zeta/dt$ values ranging from 2 to 20 ns^{-1} that were obtained for the foam-coated targets, this corresponds to a range in $\Delta\nu_{\text{axial}}$ from 0.4 to 4.0 GHz for near-normal incidence to 3.2 to 32.0 GHz for $q_0/R = 4.0$ incidence. The upper end of this range is about a factor of 10 below the bandwidth of state-of-the-art SSD systems now being implemented, which gives an asymptotic speckle-reduction effect that is about one third of that obtained with these SSD systems.

Discussion and Conclusions

The main conclusion of this article is that the optical and hydrodynamic effects of uniformly ablating plasma atmospheres in ICF experiments are capable of moving the speckled intensity distributions of phase-converted laser beams over distances that allow significant speckle reduction by time averaging. The rate at which this smoothing occurs varies widely, depending on the composition of the target and the focal convergence, incident angle, wavelength, and intensity of the irradiation. As has been shown above, smoothing times down to 100 ps and smoothing rates well within an order of magnitude of what is currently attained with SSD and ISI are possible under some circumstances. This is enough to warrant consideration of ablation-induced speckle averaging in all experiments, past and future, whose interpretations require a quantitative understanding of the effects of irradiation nonuniformity due to speckle.

For values of target and beam parameters near the nominal values considered above, the time averaging of the speckle nonuniformity due to ablation can be effective over time intervals comparable to and less than the hydrodynamic time scales typical of ICF experiments. As a practical matter, however, speckle-averaging times must be compared with the time scales of competing effects, such as the time needed to imprint the initial nonuniformity of the laser beam irreversibly into the target and the time scale of self-focusing of laser light in the atmosphere. The best generalization that can be made at this time is that ablation-induced time averaging of speckle nonuniformity is unlikely to be decisive as a means of avoiding these effects, but it is potentially significant over the time intervals during which they occur. Understanding ablation-induced speckle smoothing is essential to a complete quantitative understanding of laser-irradiation nonuniformity and its effects in ICF experiments.

An incidental conclusion to be drawn from this work is the interesting point of principle that an ablating plasma does act in some ways to avoid the detrimental effects of irradiation nonuniformity. Ablation-induced time averaging is, in fact, an unavoidable consequence of ablation. This is contrary to the more familiar tendency of ICF plasmas to exacerbate irradiation nonuniformities through the self-focusing of irradiation at intensity peaks and to misdirect the laser energy through laser-driven parametric instabilities.

A logical continuation of this work would be to repeat the calculations without the paraxial approximation. As was pointed out earlier, the paraxial approximation becomes invalid as the irradiation approaches its turning point because the refractive effects become too large. The paraxial approximation also precludes calculating the irradiation of a spherical target because the curvature of the target surface creates large angles of incidence near the limb of the irradiated hemisphere. It has been shown here that the reduction of speckle by axial averaging scales favorably with small incident angles in planar geometry, suggesting that relatively strong averaging effects might be obtained as a result of the broad range of incident angles occurring with a single beam in spherical geometry.

ACKNOWLEDGMENT

This work was supported by the U.S. Department of Energy Office of Inertial Confinement Fusion under Cooperative Agreement No. DE-FC03-92SF19460, the University of Rochester, and the New York State Energy Research and Development Authority. The support of DOE does not constitute an endorsement by DOE of the views expressed in this article.

REFERENCES

1. J. Nuckolls *et al.*, Nature **239**, 139 (1972).

2. R. L. McCrory, J. M. Soures, J. P. Knauer, S. A. Letzring, F. J. Marshall, S. Skupsky, W. Seka, C. P. Verdon, D. K. Bradley, R. S. Craxton, J. A. Delettrez, R. Epstein, P. Jaanimagi, R. Keck, T. Kessler, H. Kim, R. L. Kremens, P. W. McKenty, R. W. Short, and B. Yaakobi, Laser Part. Beams **11**, 299 (1993).

3. C. B. Burckhardt, Appl. Opt. **9**, 695 (1970); Y. Kato and K. Mima, Appl. Phys. B **29**, 186 (1982); Laboratory for Laser Energetics LLE Review **33**, NTIS document No. DOE/DP/40200-65, 1987 (unpublished), p. 1; and Laboratory for Laser Energetics LLE Review **63**, NTIS document No. DOE/SF/19460-91, 1995 (unpublished), p. 1.

4. Y. Kato *et al.*, Phys. Rev. Lett. **53**, 1057 (1984).

5. Laboratory for Laser Energetics LLE Review **64**, NTIS document No. DOE/SF/19460-99, 1995 (unpublished), p. 170.

6. R. H. Lehmberg and S. P. Obenschain, Opt. Commun. **46**, 27 (1983).

7. S. Skupsky, R. W. Short, T. Kessler, R. S. Craxton, S. Letzring, and J. M. Soures, J. Appl. Phys. **66**, 3456 (1989).

8. S. P. Obenschain *et al.*, Phys. Rev. Lett. **56**, 2807 (1986); A. N. Mostovych *et al.*, Phys. Rev. Lett. **59**, 1193 (1987); and S. P. Obenschain *et al.*, Phys. Rev. Lett. **62**, 768 (1989).

9. D. K. Bradley, J. A. Delettrez, and C. P. Verdon, Phys. Rev. Lett. **68**, 2774 (1992); H. A. Baldis *et al.*, Lawrence Livermore National Laboratory Inertial Confinement Fusion ICF Quarterly Report UCRL-LR-105821-93-3 (1993), p. 137; J. Delettrez, D. K. Bradley, and C. P. Verdon, Phys. Plasmas **1**, 2342 (1994); and D. S. Montgomery *et al.*, Phys. Plasmas **3**, 1728 (1996).

10. D. H. Kalantar, M. H. Key, L. B. DaSilva, S. G. Glendinning, J. P. Knauer, B. A. Remington, F. Weber, and S. V. Weber, Phys. Rev. Lett. **76**, 3574 (1996).

11. M. Desselberger *et al.*, Phys. Rev. Lett. **68**, 1539 (1992).

12. T. Dewandre, J. R. Albritton, and E. A. Williams, Phys. Fluids **24**, 528 (1981).

13. R. E. Kidder, Nucl. Fusion **16**, 3 (1976).

14. S. Skupsky and K. Lee, J. Appl. Phys. **54**, 3662 (1983).

15. S. E. Coe, T. Afshar-rad, and O. Willi, Opt. Commun. **73**, 299 (1989).

16. K. Okada *et al.*, Appl. Phys. Lett. **42**, 231 (1983); T. Afshar-rad *et al.*, Phys. Rev. Lett. **73**, 74 (1994); M. Desselberger *et al.*, Phys. Rev. Lett. **74**, 2961 (1995); and M. Dunne *et al.*, Phys. Rev. Lett. **75**, 3858 (1995).

17. Y. Takeda, Y. Oshida, and Y. Miyamura, Appl. Opt. **11**, 818 (1972).

18. R. Epstein and S. Skupsky, J. Appl. Phys. **68**, 924 (1990).

19. P. W. Milonni and J. H. Eberly, *Lasers* (Wiley, New York, 1988), p. 486.

20. S. Skupsky, private communication (1996).

21. K. A. Brueckner and S. Jorna, Rev. Mod. Phys. **46**, 325 (1974).